Geophysical and Astrophysical Fluid Dynamics
Vol. 00, No. 00, Month 200x, 1–8

Formation of magnetic flux tubes in cylindrical wedge geometry

G. J. J. BOTHA†, A. M. RUCKLIDGE*‡ and N. E. HURLBURT§

† Centre for Fusion, Space and Astrophysics, Physics Department, University of Warwick, Coventry CV4 7AL, UK
‡ Department of Applied Mathematics, University of Leeds, Leeds LS2 9JT, UK
§ Lockheed Martin Solar and Astrophysics Laboratory, Organization ADBS Building 252, Palo Alto, CA 94304, USA

(*Received 00 Month 200x; in final form 00 Month 200x*)

Three-dimensional (3D) magnetohydrodynamic (MHD) numerical simulations have not been able to demonstrate convincingly the spontaneous formation of large vertical flux tubes. Two-dimensional (2D) magnetoconvection in axisymmetric cylinders forms a central magnetic flux tube surrounded by annular convection rings. To study the robustness of this type of solution in three dimensions, the nonlinear resistive MHD equations are solved numerically in a 3D cylindrical wedge from an initially uniform vertical magnetic field. It is shown that the 2D result is retrieved for small domain radii. However, for larger radii the central axis loses its importance and in this case many convection cells form in the numerical domain. Magnetic flux is captured between cells where flow converges and the reduced amount of flux that congregates at the central axis is eroded by the surrounding convection.

Keywords: magnetoconvection; turbulent erosion; flux separation; numerical solution

1 Introduction

The formation of flux bundles in magnetoconvection is an important aspect in the evolution of magnetic flux in the solar convection zone and photosphere (**??**). Until now, numerical simulations have had mixed results in demonstrating the formation of large magnetic flux bundles from dispersed magnetic flux elements through the action of magnetoconvection only. The most successful in producing long-lasting pores are **?**, who produced magnetic flux bundles in intergranular lanes on a mesogranular scale. Magnetic flux was swept into vortices and then concentrated by downflows to reach maximum values of 4 kG at depths 1–4 Mm, and values of 1.5 kG at the surface. The structures lasted for the duration of the simulation (several hours). The precise mechanism for their formation was not established.

Simulations in three-dimensional (3D) Cartesian numerical domains have followed two approaches to this problem. On the one hand are simulations that include partial ionization and radiative transfer (**????**), while the other approach simplifies the physics to idealised conditions (**???????**). Whether the weak seed magnetic field is of mixed polarity (**?**) or uniform (**?**), convective motion produces highly intermittent magnetic field concentrations at the boundaries between convection cells.

In 2D cylindrical simulations of Boussinesq convection, all the initial magnetic flux in the simulation domain migrates to the central axis where it forms a central flux bundle. **?** showed that this will always be true for the Rayleigh-Bénard problem with an impenetrable outer wall, provided that the Rayleigh number is large. Compressible magnetoconvection in axisymmetric cylinders shows the same result, namely that magnetic flux in the simulation migrate to the central axis to form a flux bundle with annular convection cells surrounding it (**???**). When the 2D axisymmetric solution is used to initialise a 3D wedge shaped simulation, a remnant of the central magnetic flux bundle persists in spite of turbulent erosion due to its surrounding convection (**??**).

In this paper we consider the robustness of a magnetic flux tube forming at the central axis in a 3D cylindrical wedge domain for compressible magnetoconvection. The simulation is initialised with a uniform vertical magnetic field and allowed to evolve using the magnetohydrodynamic (MHD) equations. It will

*Corresponding author. Email: A.M.Rucklidge@leeds.ac.uk

Geophysical and Astrophysical Fluid Dynamics
ISSN: print/ISSN online
DOI:

be shown that the central axis loses its privileged position once the radial dimensions of the cylindrical wedge becomes large enough for many convection cells to form. Consequently, magnetoconvection in large 3D cylindrical wedges behaves similar as in 3D Cartesian domains. In cylindrical wedges with smaller radii the 3D calculations reproduce the axisymmetric results, that is, a central flux bundle forms on axis.

2 Model

2.1 *Equations*

The nonlinear equations for fully compressible, 3D MHD convection are solved in a 3D wedge (**?**). To these is added a hyperbolic equation in order to enforce divergence cleaning (**?**). All physical quantities are dimensionless, with length scaled to the depth of the numerical domain, velocities scaled to the sound speed at the top of the domain, and temperature, magnetic field, density and pressure all scaled to their initial values at the top of the numerical domain.

The initial magnetic field is chosen to be vertical, so that there are no Lorentz forces and an equilibrium solution exists with a vertically stratified temperature profile given by $T = 1 + \theta z$. Here θ is the initial temperature gradient and the vertical direction is given by z. The initial plasma forms a polytrope.

The dimensionless physical parameters that quantify the magnetoconvection are the Rayleigh number R, the Prandtl number σ, the Chandrasekhar number Q, the magnetic diffusivity ratio at the top of the numerical domain ζ_0, the ratio of specific heats γ, and the polytropic index m. The numerical results in this paper were obtained with the following parameter values: $R = 10^5$, $\sigma = 1$, $\zeta_0 = 0.2$, $\theta = 10$, $\gamma = 5/3$, and $m = 1.495$. The values of Q and the aspect ratio of the domain were varied and will be reported throughout the paper.

2.2 *Numerical model*

The numerical implementation of the model was developed specifically for these type of calculations (**??**). The numerial grid is in the shape of a 3D cylindridal wedge (r, ϕ, z) with depth of one unit and radius Γ. The azimuthal number $M_\phi = 2\pi/\phi_{max}$ quantifies its width. All the results presented in this paper were obtained with $M_\phi = 8$. Sixth-order compact finite differencing is used in the vertical plane with a spectral treatment in the azimuthal direction. The level of dealiasing is increased towards the central axis to maintain grid uniformity. The time evolution uses a fourth-order modified (explicit) Bulirsch-Stoer integration technique. The number of grid points in the radial direction is typically $64 \times \Gamma$, in the vertical direction 64, and in the azimuthal direction between 64 and 512.

Both top and bottom boundaries are impenetrable, set the magnetic field to be vertical and treat the temperature as fixed. The boundary condition in the azimuthal direction is periodic. At the central axis regularity conditions are imposed with no plasma flowing across $r = 0$. The numerical domain has a slippery, perfectly conducting, thermally insulating outside wall. The boundaries are described in detail in **?**.

2.3 *Diagnostic*

A quantitative measure of the breakup of the central magnetic flux tube is provided by defining the radial profile of the magnetic field as

$$|\bar{B}(r)| = \frac{1}{nz.n\phi} \sum^{nz} \sum^{n\phi} \sqrt{B_r^2 + B_\phi^2 + B_z^2}\,, \tag{1}$$

where nz and $n\phi$ are the number of data points in the vertical and azimuthal directions respectively. In order to compare the magnetisation of the plasma with different values of the Chandrasekhar number Q, we monitor $\sqrt{Q}\,|\bar{B}|$. This gives an indication of the effective magnetic field strength as a function of the

radial direction. Figures 1 and 2 present the time evolution of $\sqrt{Q}\,|\bar{B}|$ respectively for radii $\Gamma = 3$ and $\Gamma = 6$ and for different values of Q. An indication of the final state of each simulation run is given by its horizontal midplane in figure 3.

3 Discussion of results

After initialising with a uniform vertical magnetic field, magnetoconvection forms that drives flux separation in the whole of the numerical domain. The degree to which magnetic flux is separated depends on the strength of the magnetic field, given by the value of Q, and the radius of the box (Γ). The influence of the wedge width (M_ϕ) is discussed in **?**.

In all cases with $\Gamma = 3$, the convection eventually forces the majority of the magnetic flux to the central axis, similar to the axisymmetric (2D) results of **?**. Figure 1 shows this for $Q = 32$ until the time when all the magnetic flux has gathered at the central axis. The convection with $Q = 250$ is presented till long after the flux has gathered at the central axis, showing the stability of the configuration once the central flux bundle has formed. The weaker the magnetic field the more the convection dominates the solution, which leads to shorter time spans before all the magnetic flux is forced to the central axis (figure 1) and smaller final radius for the central flux bundle, as shown in figures 1 and 3(a) and (b). This corresponds to the 2D result: the higher the magnetic flux in the solution, the wider the central flux bundle. The convection is such that one convection cell forms with an inflow towards the central axis and that dominates the top half of the numerical domain. This can be seen in figure 3(a) and (b), where the inflow is clearly visible in the midplane of the numerical box. Again this corresponds to the axisymmetric result.

The 2D results of **?** show a magnetic field strength on axis of approximately double the values obtained in this 3D study. The radius of the magnetic flux bundle that forms in 3D when $\Gamma = 3$, is twice that of the axisymmetric bundle radius. This is clear when figures 1(b) and (d) are compared to figures 3(a) and (b) in **?**. The flow configuration in the simulations can explain these results. Under axisymmetry a collar flow forms around the central flux tube with an inflow at the top of the numerical domain, while there is no flow inside the magnetic flux bundle. In the 3D solutions weak flows form inside the flux bundle. These weak flows push the radius of the central flux bundle to be wider, so that the same magnetic flux ($\sqrt{Q}\,\Gamma^2$) in the solution leads to lower $\sqrt{Q}\,|\bar{B}|$ values. The weak flows inside the flux bundle push magnetic field radially outwards, so that a peak value in the magnetic field strength forms at the edge of the flux bundle, as can be seen in figures 1(b) and (d) . It follows that this peak is much more prominent in 3D than in the 2D case.

For radii of $\Gamma = 6$, the same Q values and convection strength form multiple convection cells in the radial direction, as can be seen in figure 3(c) and (d). Some of the magnetic flux is trapped between these cells where converging flows occur. Figure 2(a) and (c) show that the trapped magnetic flux does not move to the central axis in the cases with $Q = 32$ and 250. In fact, throughout the duration of the numerical run convection cells form near the central axis that force magnetic flux away from the axis.

In the case of $\Gamma = 3$, a higher value of Q leads to a larger radius of the flux bundle that forms at the central axis, as is shown in figures 1 and 3(a) and (b). In contrast, increasing Q in the numerical domain with $\Gamma = 6$ did not produce a smaller convective area around a larger central magnetic flux bundle. Instead, the stronger magnetic flux in the numerical domain forced smaller convection cells to form, which created slowly moving patterns in the numerical domain. Figures 2(e) and 3(e) show the result when $Q = 700$ is used. No central flux bundle forms, but convection cells closer to the central axis are more stable than those towards the outer radial boundary where cells change shape and morph into each other as the local magnetic flux is pushed around by the convection. This result is similar to that obtained by **?**.

The value of the magnetic flux at the central axis is approximately the same in all the numerical simulations presented in this paper, whether a central magnetic flux bundle formed or not. Figures 1(b) and (d) as well as 2(b), (d) and (f) show the effective magnetic field strength, given by $\sqrt{Q}\,|\bar{B}|$, for radii $\Gamma = 3$ and 6. The similar central magnetic flux values suggest that to increase the magnetic field strength at the central axis, one has to increase the strength of convection in the numerical simulations. This can be done by increasing the Rayleigh number R, or decreasing the Prandtl number σ. The latter resulted in

stronger convection that forced smaller time steps and denser numerical grids, as in **?**, and as such was not pursued. By increasing the strength of the convection in this way, one should be able to create a central flux bundle for $\Gamma = 6$ similar to $\Gamma = 3$.

The 3D results presented here are consistent with the 2D results of previous papers: within the context of magnetoconvection simulations, a substantial magnetic flux tube at the centre requires a pronounced inflow to maintain it. In axisymmetric simulations ($M_\phi = \infty$), the magnetic field at the central axis is confined by the surrounding inflowing annular (or toroidal) convection cells (**??**). Relaxing the axisymmetric constraint by allowing variation in the azimuthal direction in an eighth of a cylinder ($M_\phi = 8$, as presented in this paper) allows the annular cells to break up into many granular cells. Magnetic flux escapes in the lanes between the granules where there is no inflow, so that less flux remains at $r = 0$. **?** relaxed the symmetry further to $M_\phi = 4$ with $\Gamma = 3$, and observed that the granular cells grew to fill the expanded azimuthal width. In the same way higher M_ϕ values produce smaller granular convection cells. For very narrow wedges (high M_ϕ values) the solution will tend to the axisymmetric result, especially towards the axis. This effect is also seen in figures 2(e) and 3(e) with $Q = 700$.

In the $\Gamma = 3$ wedge the entire 3D solution presented here is aware of the cylindrical wedge geometry: the outer wall and the central axis. A larger radius allows granular cells to form that are shielded from the boundaries by cells next to the outer wall and near the axis, so that this part of the solution resembles Cartesian results. If a full cylindrical domain were used, with a large enough radius, we would expect that the central axis would play no distinguished role.

4 Conclusion

No 3D numerical examples exist that produce significant vertical magnetic flux bundles. In 2D axisymmetric geometry a flux bundle forms at the central axis with a collar flow surrounding it (**?**). 3D radiative models of sunspots in Cartesian coordinates (**???**) initialise the simulations with the required magnetic field configuration. Cylindrical wedge domains with large radii come close to being Cartesian because the central axis, while still present, loses its dominance.

To study 3D nonlinear magnetoconvection in cylindrical wedge geometry, a numerical domain in the form of a cylindrical wedge of width $M_\phi = 8$ is used. A uniform vertical magnetic field initialises the system, after which convection drives flux separation. For numerical domains with small radii, the 2D result is retrieved, namely that a central magnetic flux bundle forms surrounded by convection cells. However, if the radius of the cylindrical wedge is increased, the convection forms many cells with magnetic flux captured where converging flows occur. Not only does this reduce the size of the central flux bundle, but the magnetic flux at the central axis is continuously eroded by the convection surrounding it. As a result, the central axis loses its special position in the numerical solution and all magnetic flux tubes that form are transient. The maintenance of such structures in the turbulent convection must require either additional physical processes, such as flux emergence (**?**), not included in our study or reflect some external forcing.

5 Acknowledgments

GJJB and AMR would like to acknowledge financial support from NASA grant NNG04GG07G, PPARC grant PPA/G/O/2002/00014 and STFC grants PP/E001092/1, ST/F00205X/1 and ST/H002332/1. NEH would like to acknowledge support from NASA grants NNG06GD45G and NNM07AA01C. Computing facilities were provided by the White Rose Grid and the NASA supercomputer, the latter made possible through Prof. F.H. Busse.

REFERENCES

Bello González, N., Yelles Chaouche, L., Okunev, O. and Kneer, F., Dynamics of small-scale magnetic fields on the Sun: observations and numerical simulations. *Astron. Astrophys.* 2009, **494**, 1091–1106.

Botha, G.J.J., Busse, F.H., Hurlburt, N.E. and Rucklidge, A.M., Numerical simulations of rotating axisymmetric sunspots. *Mon. Not. R. Astron. Soc.* 2008, **387**, 1445–1462.

Botha, G.J.J., Rucklidge, A.M. and Hurlburt, N.E., Converging and diverging convection around axisymmetric magnetic flux tubes. *Mon. Not. R. Astron. Soc.* 2006, **369**, 1611–1624.

Botha, G.J.J., Rucklidge, A.M. and Hurlburt, N.E., Nonaxisymmetric instabilities of convection around magnetic flux tubes. *Astrophys. J.* 2007, **662**, L27–L30.

Botha, G.J.J., Rucklidge, A.M. and Hurlburt, N.E., Nonlinear three-dimensional magnetoconvection around magnetic flux tubes. *Astrophys. J.* 2011, **731**, 108.

Bushby, P.J., Magnetic fields in the solar photosphere. *Phil. Trans. R. Soc. A* 2008, **366**, 4465–4476.

Bushby, P.J., Houghton, S.M., Proctor, M.R.E. and Weiss, N.O., Convective intensification of magnetic fields in the quiet Sun. *Mon. Not. R. Astron. Soc.* 2008, **387**, 698–706.

Cattaneo, F., Emonet, T. and Weiss, N.O., On the interaction between convection and magnetic fields. *Astrophys. J.* 2003, **588**, 1183–1198.

Cheung, M.C.M., Rempel, M., Title, A.M. and Schüssler, M., Simulation of the formation of a solar active region. *Astrophys. J.* 2010, **720**, 233–244.

Danilovic, S., Schüssler, M. and Solanki, S.K., Magnetic field inensification: comparison of 3D MHD simulations with Hinode/SP results. *Astron. Astrophys.* 2010a, **509**, A76.

Danilovic, S., Schüssler, M. and Solanki, S.K., Probing quiet Sun magnetism using MURaM simulations and Hinode/SP results: support for a local dynamo. *Astron. Astrophys.* 2010b, **513**, A1.

Dedner, A., Kemm, F., Kröner, D., Munz, C.D., Schnitzer, T. and Wesenberg, M., Hyperbolic divergence cleaning for the MHD equations. *J. Comput. Phys.* 2002, **175**, 645–673.

Galloway, D.J., Proctor, M.R.E. and Weiss, N.O., Magnetic flux ropes and convection. *J. Fluid Mech.* 1978, **87**, 243–261.

Hurlburt, N.E. and Alexander, D., Sunspot dynamics and coronal heating; in *COSPAR Colloq. 14, Solar-Terrestrial Magnetic Activity and Space Environment* 2002, pp. 19–25.

Hurlburt, N.E. and Rucklidge, A.M., Development of structure in pores and sunspots: flows around axisymmetric magnetic flux tubes. *Mon. Not. R. Astron. Soc.* 2000, **314**, 793–806.

Isobe, H., Proctor, M.R.E. and Weiss, N.O., Convection-driven emergence of small-scale magnetic fields and their role in coronal heating and solar wind acceleration. *Astrophys. J.* 2008, **679**, L57–L60.

Kitiashvili, I.N., Kosovichev, A.G., Wray, A.A. and Mansour, N.N., Mechanism of spontaneous formation of stable magnetic structures on the Sun. *Astrophys. J.* 2010, **719**, 307–312.

Nordlund, Å., Stein, R.F. and Asplund, M., Solar surface convection. *Living Rev. Solar Phys.* 2009, **6**, 2.

Rempel, M., Penumbral fine structure and driving mechanism of large-scale flows in simulated sunspots. *Astrophys. J.* 2011, **729**, 5.

Rempel, M., Schüssler, M., Cameron, R.H. and Knölker, M., Penumbral structure and outflows in simulated sunspots. *Science* 2009a, **325**, 171–174.

Rempel, M., Schüssler, M. and Knölker, M., Radiative magnetohydrodynamic simulation of sunspot structure. *Astrophys. J.* 2009b, **691**, 640–649.

Rucklidge, A.M., Weiss, N.O., Brownjohn, D.P., Matthews, P.C. and Proctor, M.R.E., Compressible magnetoconvection in three dimensions: pattern formation in a strongly stratified layer. *J. Fluid Mech.* 2000, **419**, 283–323.

Stein, R.F. and Nordlund, Å., Solar small-scale magnetoconvection. *Astrophys. J.* 2006, **642**, 1246–1255.

Weiss, N.O., Umbral and penumbral magnetoconvection. *Astron. Nachr.* 2002, **323**, 371–376.

Weiss, N.O., Brownjohn, D.P., Matthews, P.C. and Proctor, M.R.E., Photospheric convection in strong magnetic fields. *Mon. Not. R. Astron. Soc.* 1996, **283**, 1153–1164.

Weiss, N.O., Proctor, M.R.E. and Brownjohn, D.P., Magnetic flux separation in photospheric convection. *Mon. Not. R. Astron. Soc.* 2002, **337**, 293–304.

Table 1. Physical parameters sampled in the vertical plane at $\phi = 0$ in figure 3.

Numerical run		β		j_ϕ		$\tilde{T}$		maximum
Q	Γ	min	max	min	max	min	max	Mach number
32	3	35.8	3.4×10^{11}	-40.7	103.7	0.98	1.01	0.08
250	3	28.0	7.8×10^{6}	-15.6	27.5	0.89	1.01	0.06
32	6	15.6	2.3×10^{11}	-100.5	79.8	0.98	1.01	0.04
250	6	20.8	2.9×10^{10}	-21.8	19.9	0.98	1.01	0.04
700	6	25.8	5.4×10^{6}	-13.6	19.2	0.99	1.01	0.03

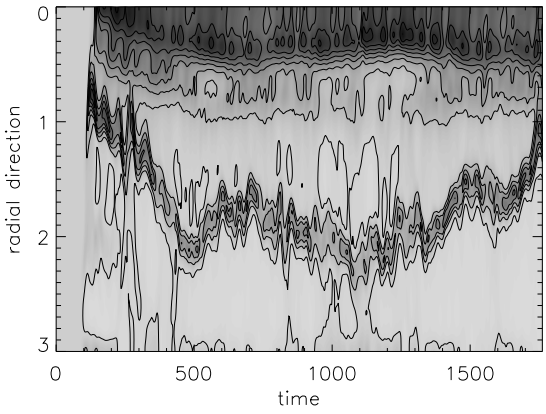

(a) $Q = 32$ with $\max(\sqrt{Q}\,|\bar{B}|) = 63.09$

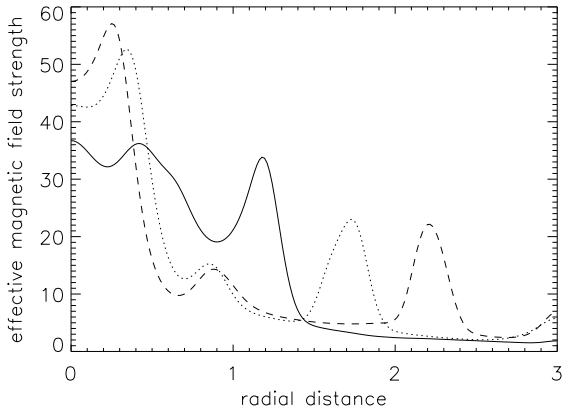

(b) Radial profile of three instances from (a). The solid line is at time 1761.09, the dotted line at 1179.1 and the broken line at 592.86.

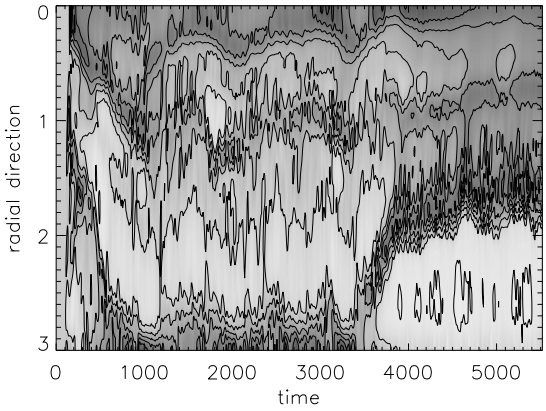

(c) $Q = 250$ with $\max(\sqrt{Q}\,|\bar{B}|) = 82.92$

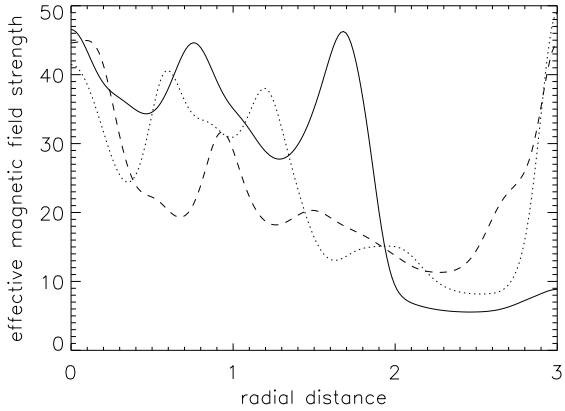

(d) Radial profile of three instances from (c). The solid line is at time 5519.43, the dotted line at 2854.31 and the broken line at 1021.85.

Figure 1. Time evolution of $\sqrt{Q}\,|\bar{B}|$ with $\Gamma = 3$. $|\bar{B}|$ is defined in (1). (a) and (c) are the time evolution with $\max(\sqrt{Q}\,|\bar{B}|)$ black and white zero. The central axis is along the top edge of each panel. (b) and (d) are three instances from the figures on the left.

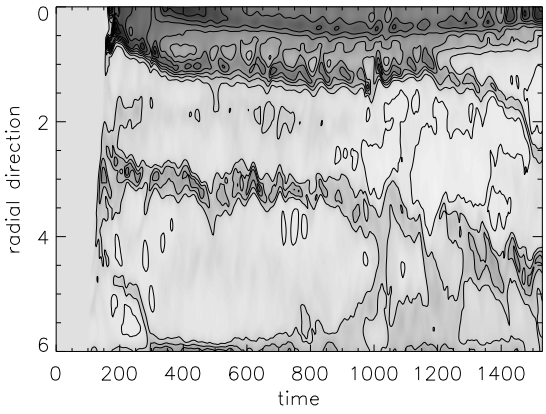

(a) $Q = 32$ with $\max(\sqrt{Q}\,|\bar{B}|) = 68.38$

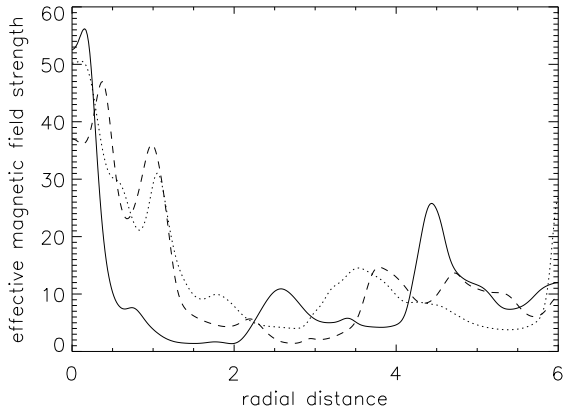

(b) Radial profile of three instances from (a). The solid line is at time 1529.45, the dotted line at 1011.42 and the broken line at 491.46.

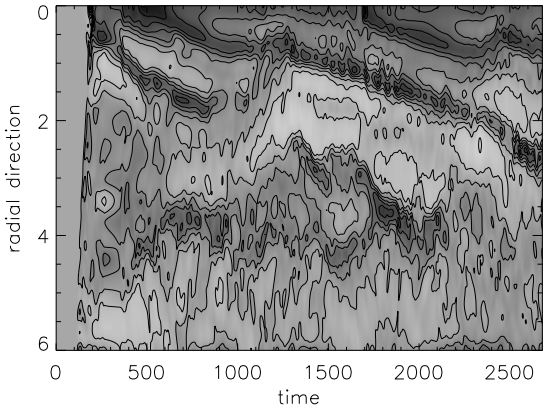

(c) $Q = 250$ with $\max(\sqrt{Q}\,|\bar{B}|) = 61.88$

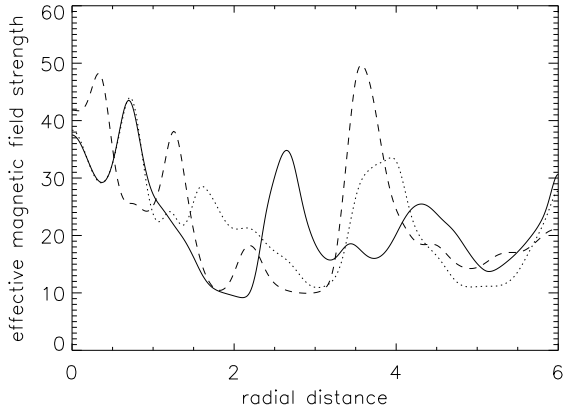

(d) Radial profile of three instances from (c). The solid line is at time 2679.2, the dotted line at 1803.25 and the broken line at 923.05.

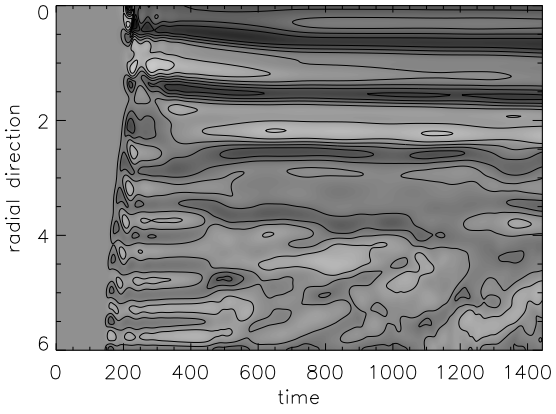

(e) $Q = 700$ with $\max(\sqrt{Q}\,|\bar{B}|) = 51.38$

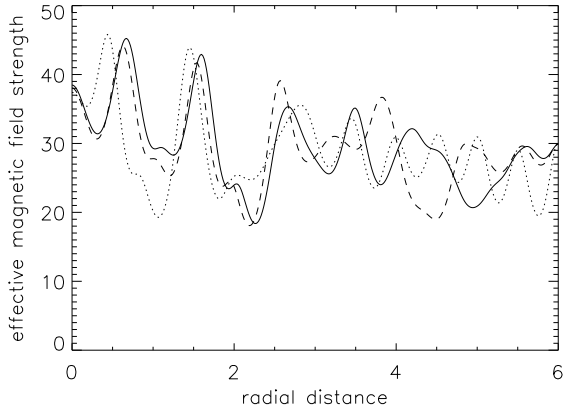

(f) Radial profile of three instances from (e). The solid line is at time 1443.92, the dotted line at 855.46 and the broken line at 391.91.

Figure 2. Time evolution of $\sqrt{Q}\,|\bar{B}|$ with $\Gamma = 6$. $|\bar{B}|$ is defined in (1). (a), (c) and (e) are the time evolution with $\max(\sqrt{Q}\,|\bar{B}|)$ black and white zero. The central axis is along the top edge of each panel. (b), (d) and (f) are three instances from the figures on the left.

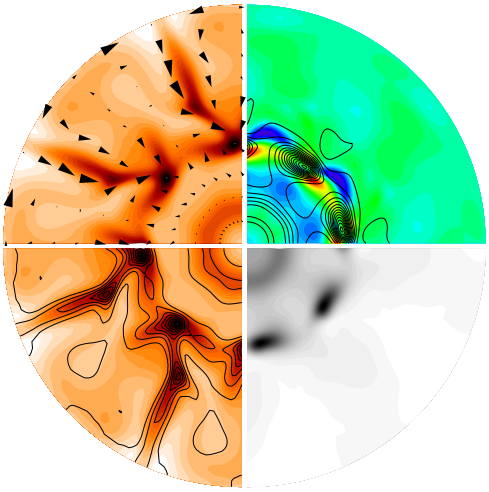

(a) $Q = 32$, $\Gamma = 3$, and $\max(\sqrt{Q}\,|\bar{B}|) = 101.25$ at time 1761.53

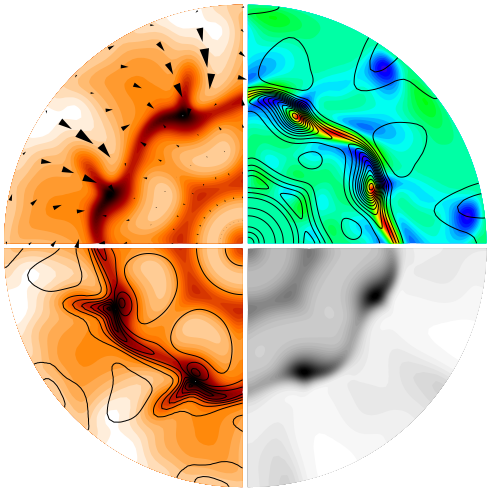

(b) $Q = 250$, $\Gamma = 3$, and $\max(\sqrt{Q}\,|\bar{B}|) = 101.25$ at time 5519.43

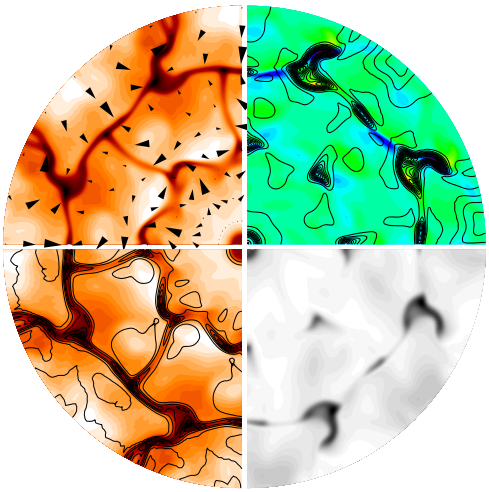

(c) $Q = 32$, $\Gamma = 6$, and $\max(\sqrt{Q}\,|\bar{B}|) = 101.25$ at time 1509.8

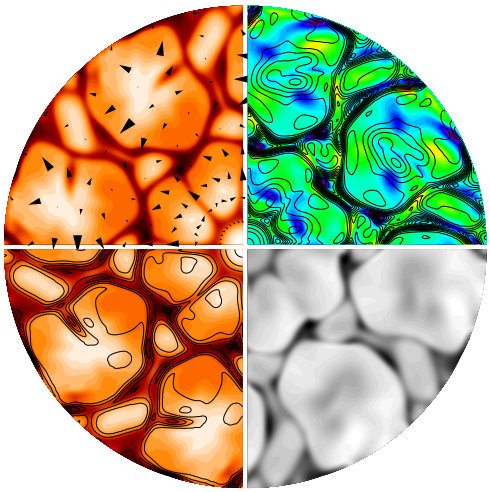

(d) $Q = 250$, $\Gamma = 6$, and $\max(\sqrt{Q}\,|\bar{B}|) = 87.15$ at time 2679.2

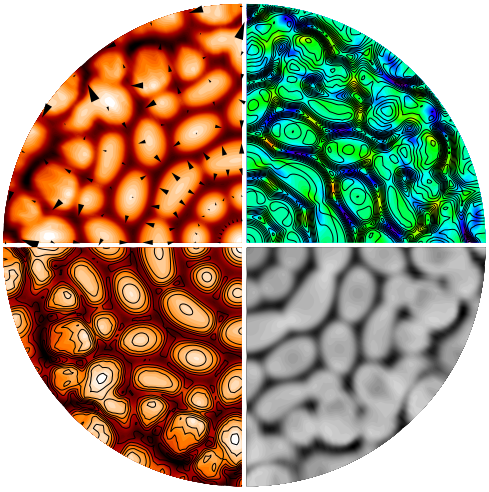

(e) $Q = 700$, $\Gamma = 6$, and $\max(\sqrt{Q}\,|\bar{B}|) = 67.07$ at time 1443.92

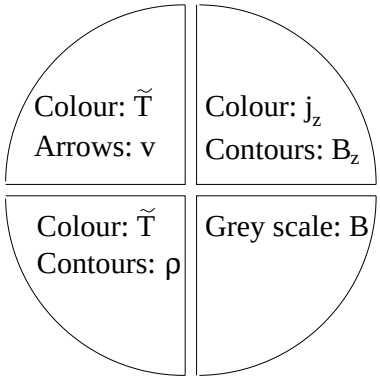

(f) Diagnostics

Figure 3. The horizontal midplane with $|\bar{B}|$ defined in (1). The diagnostics are shown in (f). In the first quadrant colour represents the axial current density j_z and contours the axial magnetic field B_z. In the second quadrant colour is the temperature fluctuation relative to the unperturbed state (dark is cold) and arrows are the velocity field. In the third quadrant colour is the temperature fluctuation relative to the unperturbed state and contours are the mass density. In the fourth quadrant grey is magnetic field strength, with maximum black